Proceedings of
ASME Turbo Expo 2011, June 6-10, 2011, Vancouver, Canada

GT2011-45437

DETACHED EDDY SIMULATION OF TRANSONIC ROTOR STALL FLUTTER USING A FULLY COUPLED FLUID-STRUCTURE INTERACTION

Hongsik IM [*], **Xiangying Chen** [†], **Gecheng Zha** [‡]
Dept. of Mechanical and Aerospace Engineering
University of Miami
Coral Gables, Florida 33124
E-mail: gzha@miami.edu

ABSTRACT

Detached eddy simulation of an aeroelastic self-excited instability, flutter in NASA Rotor 67 is conducted using a fully coupled fluid/structre interaction. Time accurate compressible 3D Navier-Stokes equations are solved with a system of 5 decoupled modal equations in a fully coupled manner. The 5th order WENO scheme for the inviscid flux and the 4th order central differencing for the viscous flux are used to accurately capture interactions between the flow and vibrating blades with the DES(detached eddy simulation) of turbulence. A moving mesh concept that can improve mesh quality over the rotor tip clearance was implemented. Flutter simulations were first conducted from choke to stall using 4 blade passages. Stall flutter initiated at rotating stall onset, grows dramatically with resonance. The frequency analysis shows that resonance occurs at the first mode of the rotor blade. Before stall, the predicted responses of rotor blades decayed with time, resulting in no flutter. Full annulus simulation at peak point verifies that one can use the multi-passage approach with periodic boundary for the flutter prediction.

1 Introduction

An self-excited aeroelastic instability, flutter can lead to mechanical failure of aircraft engine blades. The modern engines have been designed with increased pressure ratio and reduced weight in order to improve aerodynamic efficiency, resulting in severe aeroelastic problems. Particularly flutter in axial compressors with transonic flow can be characterized by a number of aerodynamic nonlinear effects such as shock boundary layer interaction, rotating stall, and tip vortex instability. Rotating blades operating under high centrifugal forces may also encounter structural nonlinearities due to friction damping and large deformations.

In the design of such highly loaded engine components, tools that can provide meaningful solutions of nonlinear effects between fluid-structure are key to success. The governing equations of structural and fluid motion have to be simultaneously integrated in time. However, due to the CPU cost, some of the fluid-structural interaction (FSI) is implemented by a loosely coupled procedure, i.e., the structural response lags behind the flow solver by one or a few time steps. The information is exchanged after partial or complete convergence of individual solvers [1]. Gnesin et al. [2] solved the unsteady Euler equations with the modal approach for the structure analysis in the partially coupled manner. Doi et al. [3] coupled an explicit Runge-Kutta multigrid flow solver with a FEM structure solver to predict the aeroelastic responses of NASA Rotor 67 blade. By Carstens eta al. [4] and Sayma et al. [5], the structural part of the governing aeroelastic equations is time-integrated according to the algorithm of Newmark, while the unsteady airloads are computed at every time step by a Navier-Stokes code.

The fully coupled fluid/structure interaction approach used in this study was validated for AGARD Wing flutter simulation by Chen et al. [6]. Time accurate 3D compressible Navier-Stokes equations are solved with a system of 5 decoupled modal equations in a fully coupled manner. In order to decouple the equation of motion for the wing structure, transformation of the structural equations to the modal coordinates are applied. The flow filed and structure always respond simultaneously by exchanging the unsteady aerodynamic force and structural displacement within each physical

---

[*] Graduate Student, AIAA Member
[†] Research Associate Professor, AIAA Member
[‡] Associate Professor, ASME Senior Member

time step via a successive iteration on the pseudo-time step.

The purpose of this paper is to develop the simulation capability of 3D flutter in a transonic rotor using high order DES and the fully coupled fluid/structure interaction. The 5th order WENO scheme for the inviscid flux and the 4th order central differencing for the viscous flux are used to accurately capture interactions between the flow and the vibrating blades. Detached-eddy simulation (DES) approach suggested by Spalart [7] is employed to better capture flutter in stall. Recently its high fidelity toward the stalled flow simulation was demonstrated by the present author in [8]. To facilitate the FSI for the transonic rotor blades with the tip speed of supersonic, an advanced moving mesh generation technique that can significantly improve mesh skewness at the rotor tip clearance was developed.

Nomenclature

a	speed of sound, $\sqrt{\gamma p/\rho}$
C_m	meridional absolute velocity, $\sqrt{C_x^2+C_r^2}$
C_x, C_θ, C_r	absolute velocities in x, θ, r direction
d	distance from the closest wall
$\mathbf{E}, \mathbf{F}, \mathbf{G}$	inviscid flux vectors in ξ, η, ζ direction
$\mathbf{E}_v, \mathbf{F}_v, \mathbf{G}_v$	viscous flux vectors in ξ, η, ζ direction
e	total energy per unit mass
J	Jacobian of the coordinate transformation
L_∞	blade chord at hub
$\mathbf{l}$	normal vector on ξ surface with its magnitude equal to the elemental surface area and pointing to the direction of increasing ξ
l_t	grid moving velocity
M_∞	reference Mach number, $\frac{U_\infty}{a_\infty}$
p_o	total pressure
Pr	Prandtl number
Pr_r	turbulent Prandtl number
$\mathbf{Q}$	conservative variable vector
q_k	total heat flux in Cartesian coordinates
R_e	Reynolds number, $\frac{\rho_\infty U_\infty L_\infty}{\mu_\infty}$
R_o	Rossby number, $\frac{\Omega L_\infty}{U_\infty}$
T_o	total temperature
U, V, W	contravariant velocities in ξ, η, ζ direction
U_∞	reference velocity
$\mathbf{V}$	relative velocity vector
V_x, V_θ, V_r	relative velocities in x, θ, r direction
y^+	dimensionless wall normal distance
α	swirl angle, $tan^{-1}(C_\theta/C_m)$
β	pitch angle, $tan^{-1}(C_r/C_x)$
Δt	physical time step
δ_{ik}	Kronecker delta function
μ_{DES}	turbulent eddy viscosity determined by DES
ν	kinematic viscosity
$\tilde{\nu}$	working variable of the S-A model related to turbulent eddy viscosity
Ω	rotor angular frequency in *radians/sec*
τ_{ik}	shear stress in Cartesian coordinates

- Flutter parameters -

b_s	bade root semi-chord
$\bar{m}$	blade mass
$\bar{V}$	frustum volume
V^*	reduced velocity, $\frac{U_\infty}{b_s\omega_\alpha}$
V_f	flutter speed index, $\frac{V^*}{\bar{\mu}}$
ω_α	1st torsional mode natural frequency
$\bar{\mu}$	mass ratio, $\frac{\bar{m}}{\bar{V}\rho_\infty}$

2 Aerodynamic Model

An accurate Riemann solver is necessary to capture the shock wave turbulent boundary layer interaction in aeroelastic analysis. The Low Diffusion E-CUSP (LDE) Scheme [9] is used to evaluate the inviscid fluxes. The LDE scheme can capture crisp shock profile and exact contact surface discontinuities as accurately as the Roe scheme [9]. However, it is simpler and more CPU efficient than the Roe scheme due to no matrix operation. The 5th order WENO scheme for the inviscid flues and 4th order central differencing scheme for viscous terms [10] are used. An implicit unfactored Gauss-Seidel line iteration is used to achieve high convergence rate. The high-scalability parallel computing is applied to save wall clock time [11]. The DES of Spalart [7] developed based on the Spalart-Allmaras one equation model is employed.

2.1 Governing Equations

The equation of motion of fluid flow for turbomachinery in a relative frame of reference can be derived by adding the effects of coriolis force ($2\Omega\times\mathbf{V}$) and the centrifugal force($\Omega\times\Omega\times\mathbf{r}$) to the equation for the absolute frame. Expanding this momentum equation with continuity and energy equations in a rotating Cartesian system(x, y, z) as shown in Fig. 1 and applying coordinate transformation to the generalized coordinate system(ξ, η, ζ), the dimensionless spatially filtered 3D Navier-Stokes equations can be expressed as the following conservative form:

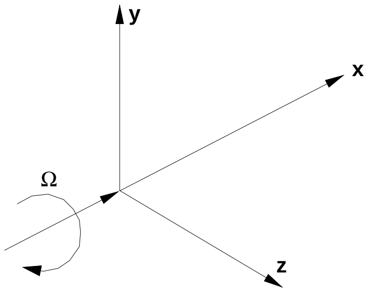

FIGURE 1: The Cartesian system with y and z axes rotation about the x-axis at a constant speed Ω

$$\frac{\partial \mathbf{Q}}{\partial t}+\frac{\partial \mathbf{E}}{\partial \xi}+\frac{\partial \mathbf{F}}{\partial \eta}+\frac{\partial \mathbf{G}}{\partial \zeta}=\frac{1}{Re}\left(\frac{\partial \mathbf{E}_v}{\partial \xi}+\frac{\partial \mathbf{F}_v}{\partial \eta}+\frac{\partial \mathbf{G}_v}{\partial \zeta}\right)+\mathbf{S} \tag{1}$$

The inviscid flux vector $\mathbf{E}$, the viscous flux vector $\mathbf{E_v}$ and the source term vector $\mathbf{S}$ are expressed as follows and the rest can be expressed following the symmetric rule.

$$\mathbf{E}=\begin{pmatrix} \bar{\rho}U \\ \bar{\rho}\tilde{u}U+l_x\bar{p} \\ \bar{\rho}\tilde{v}U+l_y\bar{p} \\ \bar{\rho}\tilde{w}U+l_z\bar{p} \\ (\bar{\rho}\tilde{e}+\bar{p})\,U-l_t\bar{p} \\ \bar{\rho}\tilde{\nu}U \end{pmatrix} \tag{2}$$

$$\mathbf{E_v}=\begin{pmatrix} 0 \\ l_k\bar{\tau}_{xk} \\ l_k\bar{\tau}_{yk} \\ l_k\bar{\tau}_{zk} \\ l_k\left(\tilde{u}_i\bar{\tau}_{ki}-\bar{q}_k\right) \\ \frac{\bar{\rho}}{\sigma}\left(\nu+\tilde{\nu}\right)\left(\mathbf{l}\bullet\nabla\tilde{\nu}\right) \end{pmatrix} \tag{3}$$

$$\mathbf{S}=\frac{1}{J}\begin{pmatrix} 0 \\ 0 \\ \bar{\rho}{R_o}^2y+2\bar{\rho}R_ow \\ \bar{\rho}{R_o}^2z-2\bar{\rho}R_ov \\ 0 \\ \bar{\rho}C_{b1}\left(1-f_{t2}\right)\tilde{S}\tilde{\nu}+ \\ \frac{1}{Re}\left[-\bar{\rho}\left(C_{w1}f_w-\frac{C_{b1}}{\kappa^2}f_{t2}\right)\left(\frac{\tilde{\nu}}{d}\right)^2\right. \\ \left.+\frac{\bar{\rho}}{\sigma}C_{b2}\left(\nabla\tilde{\nu}\right)^2-\frac{1}{\sigma}\left(\nu+\tilde{\nu}\right)\nabla\tilde{\nu}\bullet\nabla\bar{\rho}\right] \\ +Re\left[\bar{\rho}f_{t1}\left(\Delta q\right)^2\right] \end{pmatrix} \tag{4}$$

where the overbar denotes the spatial filtered quantity, and the tilde is used to denote the Favre filtered quantity. U, V and W are the contravariant velocities in ξ, η, ζ directions. For an example, U is defined as follows.

$$U=l_t+\mathbf{l}\bullet\mathbf{V}=l_t+l_x\tilde{u}+l_y\tilde{v}+l_z\tilde{w} \tag{5}$$

$$l_t=\frac{\xi_t}{J}d\eta d\zeta, \quad l=\frac{\nabla\xi}{J}d\eta d\zeta \tag{6}$$

When the grid is stationary, $l_t=0$. In the current discretization, $d\eta=d\zeta=1$.

The shear stress $\bar{\tau}_{ik}$ and total heat flux $\bar{q}_k$ in Cartesian coordinates is given by

$$\bar{\tau}_{ik}=\left(\mu+\mu_{DES}\right)\left[\left(\frac{\partial\tilde{u}_i}{\partial x_k}+\frac{\partial\tilde{u}_k}{\partial x_i}\right)-\frac{2}{3}\delta_{ik}\frac{\partial\tilde{u}_j}{\partial x_j}\right] \tag{7}$$

$$\bar{q}_k=-\left(\frac{\mu}{Pr}+\frac{\mu_{DES}}{Pr_t}\right)\frac{\partial\tilde{T}}{\partial x_k} \tag{8}$$

where μ is determined by Sutherland's law. The above equations are in the tensor form, where the subscripts i,k represents the coordinates x,y,z and the Einstein summation convention is used. Eq.(7) and (8) are transformed to the generalized coordinate system. The turbulent eddy viscosity μ_{DES} is given by

$$\mu_{DES}=\bar{\rho}\tilde{\nu}f_{v1} \tag{9}$$

where

$$f_{v1}=\frac{\chi^3}{\chi^3+c_{v1}^3}, \quad \chi=\frac{\tilde{\nu}}{\nu}$$
$$r=\frac{\tilde{\nu}}{R_e\tilde{S}k^2d^2}, \quad \tilde{S}=S+\frac{\tilde{\nu}}{R_ek^2d^2}f_{v2}, \quad f_{v2}=1-\frac{\chi}{1+\chi f_{v1}}$$
$$S=\sqrt{2\Omega_{ij}\Omega_{ij}}, \quad \Omega_{ij}=\frac{1}{2}\left(\frac{\partial u_i}{\partial x_j}-\frac{\partial u_j}{\partial x_i}\right)$$

The rest of auxiliary relations and the values of the coefficients given by reference [12] are used.

In DES, a modification of a SA based RANS model in which the model switches to a subgrid scale formulation in regions fine enough for LES calculations. The coefficients c_{t1} and c_{t3} in the SA model are set to zero and the distance to the nearest wall, d, is replaced by $\tilde{d}$ as

$$\tilde{d}=min(d,C_{DES}\Delta) \tag{10}$$

where Δ is the largest spacing of the grid cell in all the directions. Within the boundary layer close to the wall, $\tilde{d}=d$, hence the turbulence is simulated by RANS mode of Spalart-Allmaras [12]. Away from the boundary layer, $\tilde{d}=C_{DES}\Delta$ is most of the cases. When the production and destruction terms of the model are balanced, the length scale $\tilde{d}$ will have a Smagorinsky-like eddy viscosity and the turbulence is simulated by the LES model. The coefficient $C_{DES}=0.65$ is used as set in the homogeneous turbulence [13]. The Pr_t may take the value of 0.9 within the boundary layer for RANS mode and 0.5 for LES mode away from the wall surface.

The equation of state as a constitutive equation relating density to pressure and temperature in the relative frame is defined as

$$\bar{\rho}\tilde{e}=\frac{\bar{p}}{(\gamma-1)}+\frac{1}{2}\bar{\rho}(\tilde{u}^2+\tilde{v}^2+\tilde{w}^2)-\frac{1}{2}\bar{\rho}r^2\Omega^2 \tag{11}$$

where r $(= \sqrt{y^2+z^2})$ is the radius from the rotating axis, x in this study. For simplicity, all the bar and tilde in above equations will be dropped in the rest of this paper.

2.2 Implicit Time Marching Scheme

The 2nd order implicit method is used with the dual time stepping method [10, 14]. A pseudo temporal term $\frac{\partial Q}{\partial \tau}$ is added to the governing equation Eq. (1). This term vanishes at the end of each physical time step, and has no influence on the accuracy of the solution. The pseudo temporal term is discretized with first order Euler scheme. Let m stand for the iteration index within a physical time step, the semi-discretized governing equation can be expressed as

$$\begin{aligned}\left[\left(\tfrac{1}{\Delta\tau}+\tfrac{1.5}{\Delta t}\right)I-\left(\tfrac{\partial R}{\partial \mathbf{Q}}\right)^{n+1,m}\right]\delta\mathbf{Q}^{\mathbf{n+1,m+1}}\\ = R^{n+1,m}-\tfrac{3\mathbf{Q}^{\mathbf{n+1,m}}-4\mathbf{Q}^{\mathbf{n}}+\mathbf{Q}^{\mathbf{n-1}}}{2\Delta t}\end{aligned} \tag{12}$$

where $\Delta\tau$ is the pseudo time step, and R is the net flux of the discretized Navier-Stokes equations.

3 Boundary Conditions

It is convenient for turbomachinery to express the boundary conditions in Cylindrical system. Coordinates mapping between the Cartesian (x,y,z) and Cylindrical system(x,θ,r) is given as

$$\begin{pmatrix}V_x\\ V_\theta\\ V_r\end{pmatrix}=\begin{pmatrix}u\\ v\cdot sin\theta-w\cdot cos\theta\\ v\cdot cos\theta+w\cdot sin\theta\end{pmatrix}=\begin{pmatrix}u\\ \frac{v\cdot z-w\cdot y}{r}\\ \frac{v\cdot y+w\cdot z}{r}\end{pmatrix} \tag{13}$$

where u, v, and w are the relative velocity components in the x, y, and z coordinate directions respectively. The absolute velocity components(C_x,C_θ,C_r) are related to the relative velocity components(V_x,V_θ,V_r) using the rotor wheel speed$(r\Omega)$ as

$$\begin{pmatrix}C_x\\ C_\theta\\ C_r\end{pmatrix}=\begin{pmatrix}V_x\\ V_\theta-r\Omega\\ V_r\end{pmatrix} \tag{14}$$

At the rotor inlet, the radial distributions of total pressure P_o, total temperature T_o, swirl angle α and pitch angle β are specified from the experiment [15]. The velocity is taken from the computational domain by the extrapolation in order to determine the rest of variables. First, we assume that the speed of sound a is constant at the inlet boundary. Then, the static temperature is obtained by

$$T_b = T_o[1-\frac{\gamma-1}{2}(\frac{C_i}{a_o})^2] \tag{15}$$

where the subscripts i represents the first interior cell and subscripts b indicates the first ghost cell of the boundary. C_i is the absolute velocity of the first interior cell and a_o is the total speed of sound defined by

$$\frac{a_o^2}{\gamma-1}=\frac{a_i^2}{\gamma-1}+\frac{C_i^2}{2} \tag{16}$$

Using the isentropic relations, the absolute velocity(C_b), the static pressure(p_b) and density(ρ_b) are determined by

$$|C_b| = \frac{1}{M_\infty}\sqrt{\frac{2}{\gamma-1}(T_o-T_b)} \tag{17}$$

$$p_b = P_o\left(\frac{T_b}{T_o}\right)^{\frac{\gamma}{\gamma-1}} \tag{18}$$

$$\rho_b = \frac{p_b\gamma}{a_b^2} \tag{19}$$

Then, the velocity components are decoupled and the conservative variables are found as the following:

$$\begin{pmatrix}\rho\\ \rho V_x\\ \rho V_r\\ \rho V_\theta\\ \rho e\end{pmatrix}_b=\begin{pmatrix}\rho_b\\ \rho_b C_m\cdot cos\beta\\ \rho_b C_m\cdot sin\beta\\ \rho_b(C_m\cdot tan\alpha-r\Omega)\\ \frac{p_b}{(\gamma-1)}+\frac{\rho_b}{2}(V_x^2+V_r^2+V_\theta^2-r^2\Omega^2)\end{pmatrix} \tag{20}$$

At the rotor outlet, the static pressure(p_b) is specified. The components of velocity(u,v,w) are extrapolated from the computational domain. The radial distributions of the static pressure from the experiment [15] is used for the single passage validation. For the rotating stall simulations, the pressure at the peak of the rotor speed line is applied for the back pressure condition since axial compressors operating near the peak of their pressure rise characteristic have the potential to induce rotating stall [16–18]. Then, the radial distributions of the back pressure are determined by solving the simplified radial equilibrium equation(21) that can reflect the nonuniform variations of the static pressure across the full annulus.

$$\frac{1}{\rho}\frac{\partial p_b}{\partial r}=\frac{V_\theta^2}{r}=\frac{(vz-wy)^2}{r^3} \tag{21}$$

Then, to update the density(ρ_b) by using the following isentropic relation.

$$\rho_b = \left(\frac{p_b}{p_i}\right)^{\frac{1}{\gamma}} \rho_i \tag{22}$$

where p_i is the static pressure and ρ_i is the density at the first interior cell of the outlet boundary. The total energy is updated based on p_b and ρ_b.

On the solid wall, the non-slip boundary condition is applied to enforce mass flux going through the wall to be zero. The velocity components of the ghost cells are obtained by the extrapolation between the moving wall velocity and interior cells as follows:

$$\vec{V}_b = 2\vec{V}_w - \vec{V}_i \tag{23}$$

where $\vec{V}_b$ denotes the ghost cell velocity, $\vec{V}_i$ stands for the velocity of 1*st* interior cell close to the wall, and $\vec{V}_w$ is wall moving velocity given by $\vec{\Omega} \times \vec{r}$. Another option to save mesh size in our computation is to use the law of the wall. When y^+ is between 11 and 300, the no slip condition is replaced by using the wall function.

$$u^+ = \frac{1}{k} lny^+ + B \tag{24}$$

where k denotes Von K*á*rm*á*n constant taken as 0.41, and B denotes a dimensionless constant corresponding to the wall roughness taken as 5.0. If the wall surface is η direction, the wall static pressure for the inviscid momentum equation can be determined by solving Eq. (21) in the following manner:

$$\frac{\partial p}{\partial \eta} = \frac{\rho_i}{\sqrt{\eta_x^2+\eta_y^2+\eta_z^2}} \frac{V_\theta^2}{r} \tag{25}$$

If the wall surface is stationary, then the static pressure gradient across the wall boundary is set to zero. For addition, the adiabatic condition($\partial T/\partial \eta = 0$) is used to impose zero heat flux through the wall.

4 Structural Model

For the rotating blades in the relative frame of reference, on can assume that the stiffness of the rotor disk is much larger than that of the compressor blades, the vibration characteristics of the blades is dominant such that rotor disk vibration effects are negligible. The center of the rotor disk is aligned to the rotating axis, as a result no whirling effects exist. No translational acceleration of arbitrary frame of reference to absolute frame and constant rotational speed are considered.

4.1 Modal Approach

The equation of motion of an N-DOF(degree of freedom) system with the mechanical damping and the aerodynamic loading as the excitation force can be presented in matrix form:

$$[\mathbf{M}]\{\ddot{\mathbf{X}}\} + [\mathbf{C}]\{\dot{\mathbf{X}}\} + [\mathbf{K}]\{\mathbf{X}\} = \{\mathbf{F}\} \tag{26}$$

where, **M**, **C**, **K** are the mass, structural damping and stiffness matrices. **F** is total aerodynamic force acting on the blade surface. Total aerodynamic force can be defined as follows:

$$\mathbf{F} = -\oint P \cdot \hat{n} dA + \oint \tau_\mathbf{w} \cdot \hat{t} dA \tag{27}$$

where, $\hat{n}$ is the unit normal vector to the blade surface and $\hat{t}$ is the unit tangent vector to the blade surface. P is the fluid static pressure and $\tau_\mathbf{w}$ is the fluid wall shear stress acting on the blade surface. Eq. (11) is used to compute static pressure of rotor blade surface by setting flow velocity components to zero. It is likely that the effects of viscosity may not be neglected for the highly loaded transonic rotor because rotating stall with large structure of flow separation may occur in/near stall conditions.

To decouple the equations of motion for the damped systems(26), we use the mass normalized mode shape($\tilde{\phi}$) defined as the normal modes divided by square root of the the generalized mass($\sqrt{\phi^T m \phi}$). Let $\{\mathbf{X}\} = [\tilde{\Phi}]\{\mathbf{q}\}$ and premultiply Eq. (26) by the transpose $[\tilde{\Phi}]^T$.

$$\begin{aligned}[\tilde{\Phi}]^T[\mathbf{M}][\tilde{\Phi}]\{\ddot{\mathbf{q}}\} + [\tilde{\Phi}]^T[\mathbf{C}][\tilde{\Phi}]\{\dot{\mathbf{q}}\} + [\tilde{\Phi}]^T[\mathbf{K}][\tilde{\Phi}]\{\mathbf{q}\} \\ = [\tilde{\Phi}]^T\{\mathbf{F}\}\end{aligned} \tag{28}$$

where **q** is the vector of the principal coordinates. By the orthogonality of the system matrices and assuming damping matrix to be a linear combination of the mass and stiffness matrices, Eq. (28) is then completely decoupled and *j*th equation will have the form

$$\ddot{q}_j + 2\zeta_j\omega_j\dot{q}_j + \omega_j^2 q_j = \frac{\tilde{\phi}_j^T}{m_j}\mathbf{F} \tag{29}$$

where $[\tilde{\Phi}]^T = [\tilde{\phi}_1, \cdots, \tilde{\phi}, \cdots, \tilde{\phi}_N]^T$. N is the number of modal coordinates. ω_j and ζ_j are natural frequency and modal damping ratio for mode j. m_j denotes the *j*th diagonal element of modal mass matrix which will be unity. In the current study, the structural system may be reduced to only five mode shapes, since a few bending and torsional frequencies are usually sufficient to determine flutter. The normalized modal equation can be given as

$$\ddot{q}_j + 2\zeta_j(\frac{\omega_j}{\omega_\alpha})\dot{q}_j + (\frac{\omega_j}{\omega_\alpha})^2 q_j = \frac{\tilde{\phi}_j^{*T}}{m_j^*} \cdot \mathbf{F}^* \cdot {V_f}^2 \cdot \frac{b_s^2 L_\infty}{\bar{V}} \cdot \bar{m} \tag{30}$$

where the dimensionless quantities are denoted by an asterisk. $V_f (= \frac{U_\infty}{b_s \omega_\alpha \sqrt{\bar{\mu}}})$ is the flutter speed index which is an input flutter control parameter. $\bar{m}$ is the measured blade mass, $\bar{V}$ represents the conical frustum volume and b_s is the streamwise root semi chord. L_∞ is the reference length and ω_α is the angular frequency of the first torsional mode in units *radians/sec*. $\bar{\mu} (= \frac{\bar{m}}{\bar{V} \rho_\infty})$ stands for the mass ratio, i.e. the ratio between the structural mass and the mass of the equivalent volume of fluid at reference density. It is noticed that m_j^* should equal one when the mass normalized mode shapes are used.

The equations are then transformed to a state form as follows:

$$[\mathbf{M}] \frac{\partial \mathbf{S}}{\partial t} + [\mathbf{K}]\{\mathbf{S}\} = \mathbf{q} \tag{31}$$

where

$$\mathbf{S} = \begin{pmatrix} q_j \\ \dot{q}_j \end{pmatrix}, \mathbf{M} = [I], \mathbf{K} = \begin{pmatrix} 0 & -1 \\ (\frac{\omega_j}{\omega_\alpha})^2 & 2\zeta_j (\frac{\omega_j}{\omega_\alpha}) \end{pmatrix}$$

$$\mathbf{q} = \begin{pmatrix} 0 \\ \phi_j^{*T} \cdot \mathbf{F}^* \cdot V_f \cdot \frac{b_s^2 L}{\bar{V}} \cdot \bar{m} \end{pmatrix}$$

4.2 Implicit Structural Solver

To solve the structural equations with CFD solver in the fully coupled manner, the decoupled structural equations are integrated in a manner consistent with flow governing equations(12) in each physical time step :

$$\begin{aligned} &\left(\tfrac{1}{\Delta\tau} I + \tfrac{1.5}{\Delta t} M + K\right) \delta S^{n+1,m+1} \\ &= Q^{n+1,m+1} - M \tfrac{3S^{n+1,m} - 4S^n + S^{n-1}}{2\Delta t} - K S^{n+1,m} \end{aligned} \tag{32}$$

The fluid/structural interaction is implemented in a fully coupled manner [6]. Within each physical time step, the flow equations and structural equations are solved iteratively until the prescribed convergence criteria is satisfied for both flow and structural solver. After the convergence criteria is reached, the fluid-structural interaction goes to next physical time step.

5 Moving Mesh

A CPU efficient moving mesh technique is one of requisites for FSI to accurately describe the vibration of structure. The conventional method in general regenerates inside domain mesh with the fixed outer boundaries. However, this may cause significant numerical instability because of the high mesh skewness when the moving structure is close to the boundaries like rotor tip clearance. In this paper an advanced moving mesh concept as seen in Fig. 2 was developed to improve mesh quality over rotor tip clearance.

In summary, new -coordinate, x'_{casing} on the casing surface of the rotor tip block boundary is found using Eq. (33).

$$x'_{casing} = x^o_{tip} + u_{x/tip} + \Delta U_x \tag{33}$$

where

$$\Delta U_x = \frac{S_{casing} - S_{tip}}{S_{tip} - S_{tip-1}} (u_{x/tip} - u_{x/tip-1})$$

where x^o_{tip} represents the initial x-coordinate of rotor tip boundary. ΔU_x is the amount of displacements to be moved in the x-direction obtained by the extrapolation. The subscript, $_{tip-1}$ denotes the grid one point below of rotor tip surface. S is the distance from the rotor axis to corresponding coordinates. Next, new radius, $R'_{casing} (= \sqrt{{y'_{casing}}^2 + {z'_{casing}}^2})$ corresponding x'_{casing} is found by the interpolation of the given (x_o, R_{casing}). Finally y'_{casing} and z'_{casing} determined by Eq. (33) are updated using R'_{casing} as follow:

$$\begin{aligned} y'_{casing} &= R'_{casing} cos(\theta) \\ z'_{casing} &= R'_{casing} sin(\theta) \end{aligned} \tag{34}$$

where

$$\theta = tan^{-1} (\frac{z^o_{casing}}{y^o_{casing}})$$

Moving mesh generation for the rest of casing surface is completed borrowing an idea suggested by Chen et al. [6], and again projected toward the given (x_o, R_{casing}) to make sure all new points be placed on the design casing surface. Once the casing surface is obtained, regeneration of inner mesh is straightforward. The deformed mesh of a blade-to-blade surface is first obtained, and radially stacked from the blade hub to the casing. The mesh near blade is simply moved with the blade surface.

6 Flutter Control Parameters

There are in general three flutter control(or input) parameters: mass ratio($\bar{\mu} = \frac{\bar{m}}{\bar{V} \rho_\infty}$), reduced velocity($V^* = \frac{U_\infty}{b_s \omega_\alpha}$), and flutter speed index($V_f = \frac{V^*}{\bar{\mu}}$). Mass ratio can consider($\bar{\mu}$) the effect of stiffness in flutter. It represents the ratio between the structural mass and the mass of the equivalent volume of fluid at reference density. Reduced velocity(V^*) stands for the ratio of time taken for a fluid particle to flow past the length of a semi-chord to the time taken for the airfoil. Typically flutter speed index(V_f) is selected as a main parameter in flutter boundary prediction because

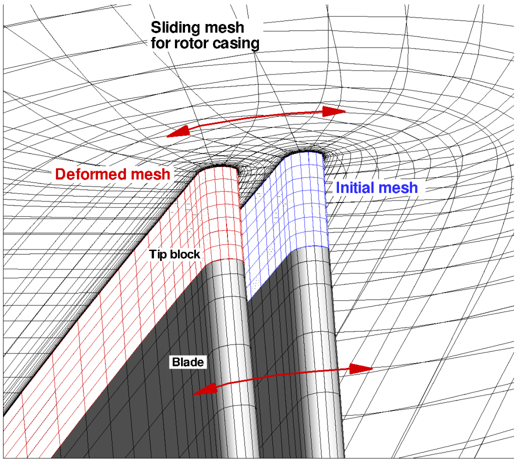

FIGURE 2: Moving mesh with sliding rotor casing

TABLE 1: NASA rotor 67 design specifications

Quantity	Value
Number of rotor blades	22
Rotational speed [rpm]	16043
Design mass flow rate [kg/s]	33.25
Measured choke mass flow [kg/s]	34.96
Design pressure ratio	1.63
Tip speed [m/s]	429
Tip relative mach number	1.38
Tip diameter at inlet/exit [mm]	514/485
Hub-tip ratio at inlet/outlet	0.375/0.478
Tip clearance [mm]	1.1
Rotor aspect ratio	1.56

V_f can reflect the effects of both the altitude and stiffness. The effects of aircraft altitude by wind tunnel tests [19,20] is understood based on variation in dynamic pressure(varying the density) at constant Mach number. Liu [21] and Chen [6] used V_f, whereas Bakhle [22] used V^* in order to find out the flutter boundary at a given Mach number. In this study, either V_f or V^* can be used explicitly as stated in Eq. (30).

7 Results and Discussion

The design specifications of Rotor 67 are summarized in table 1 and the details in experiment are reported by Strazisar et al. [15]. Flutter simulations were conducted at total 8 different operating conditions including choke, peak, and near stall. Several rotor revolutions are needed to see whether the responses are divergent or damped with time. Full annulus flutter simulation at peak condition was performed in order to validate the 4 blade passage simulation with periodic boundary condition. The value of modal damping typically determined by experiment is very small, on the order of 1 $\sim$ 3 percent of critical damping. In the current study, a uniform damping ratio of 0.005 is used for rotor flutter simulation. The effects of dynamic pressure changes in NASA Rotor 67 flutter was investigated by varying reduced velocity(V^*).

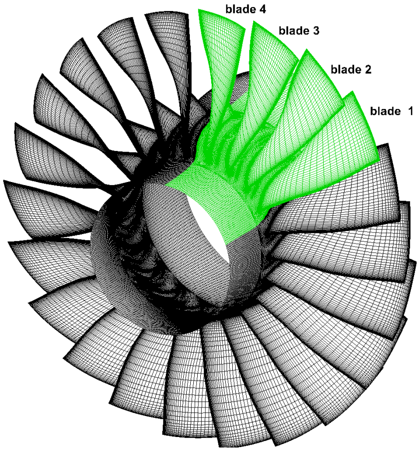

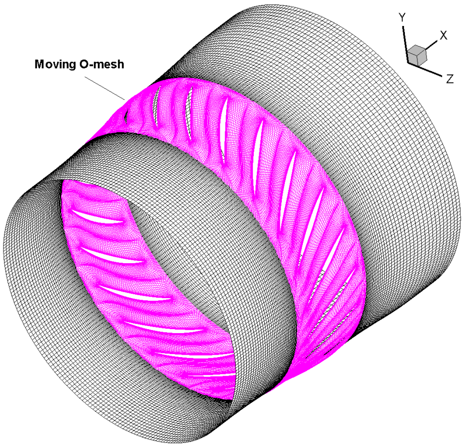

FIGURE 3: Full annulus mesh of NASA Rotor 67 constructed by using H-O-H mesh topology

7.1 4 Blade Passage Simulation

Using the 4 Blade Passages, computations for investigating flutter in NASA Rotor 67 was first performed. 8 points including choke, peak, and near stall and stall were considered. The unsteady simulations are started with the initial solution obtained by each steady state calculation. The residual is reduced three orders of magnitude in each physical time step. The physical time step, 0.0025revs(rotor revolutions) with a CFL number of 2 is used. Periodic boundary conditions are used at lower and upper boundary of the blade passage. The focus of NASA Rotor 67 flutter simulation is to investigate flutter behavior, in particular flutter boundary at the design speed of 16043 RPM. Using the design conditions in table 1, the estimated mass ratio($\bar{\mu}$) is 4299.5, and the reduced velocity(V^*) is about 0.4357.

Fig. 3 shows the full annulus mesh for NASA Ro-

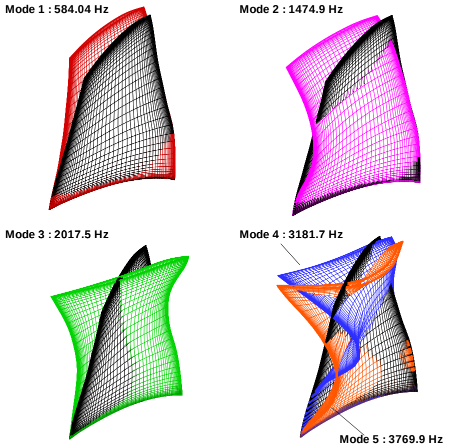

FIGURE 4: First five mass normalized mode shapes of NASA Rotor 67 obtained by ABAQUS

tor 67 constructed by applying the H-O-H mesh topology. For the 4 blade flutter FSI computations, the part of 4 blade(blade1 ∼ blade 4) in the full annulus mesh was taken. The single passage mesh has 121(around blade)×77(blade-to-blade)×47(span). A fully gridded tip model with nominal tip clearance, an O-grid with mesh size of 121×12×9, was used. The mesh uses 8 points in the spanwise direction to resolve tip clearance flow. The 1st grid spacing on the the blade surface was set to 5×10^5 times the blade hub chord length which gives $y^+ < 5$, while on the hub and casing surface it was set to 2×10^3 times blade hub chord which can give y+ around 50. Therefore, the wall function BCs [23] are used on the hub and casing. Total 56 blocks were used for the parallel computation.

The first five mode shapes normalized by the generalized mass as displayed in Fig. 4 was obtained by using ABAQUS. The rotor blades were assumed as titanium alloy properties with Young's modulus=1.172×10^{11} Pa, Poisson's ratio=0.3, and density 4539 kg/m^3 since the material properties used in original design were not reported. The centrifugal force effects were considered. The blades are modeled as fixed at the rigid body rotor. The grid data on the blade surface used in CFD mesh were taken in ABAQUS FE modeling. The first five natural frequencies of Rotor 67 is 584.04 Hz, 1474.9 Hz, 2017.5 hz, 3181.7 Hz, and 3789.9 Hz. For the normal operating condition with 16043 RPM, the blade passing frequency(BPF) is 5882.4 Hz.

Fig. 5 shows the modal displacements of the second blade at choke, peak and near stall. It is clearly shown that the blade oscillations decay with time, resulting in no flutter at choke, peak and near stall. The amplitude level at near stall is larger than those at choke and peak even though the mass flow through the compressor decreases toward stall.

Fig. 6 displays the normalized surface static pressure distributions of a rotor blade(the second blade) at 50% span. It is obvious that the static pressure and its difference between the rotor pressure surface and suction suction surface increases toward stall, as a result increased blade loading and displacements. The modal displacements at near stall are compared in Fig. 7. Blade 1, 2, 3 and 4 vibrate with almost same level of phase angles and amplitudes without flutter.

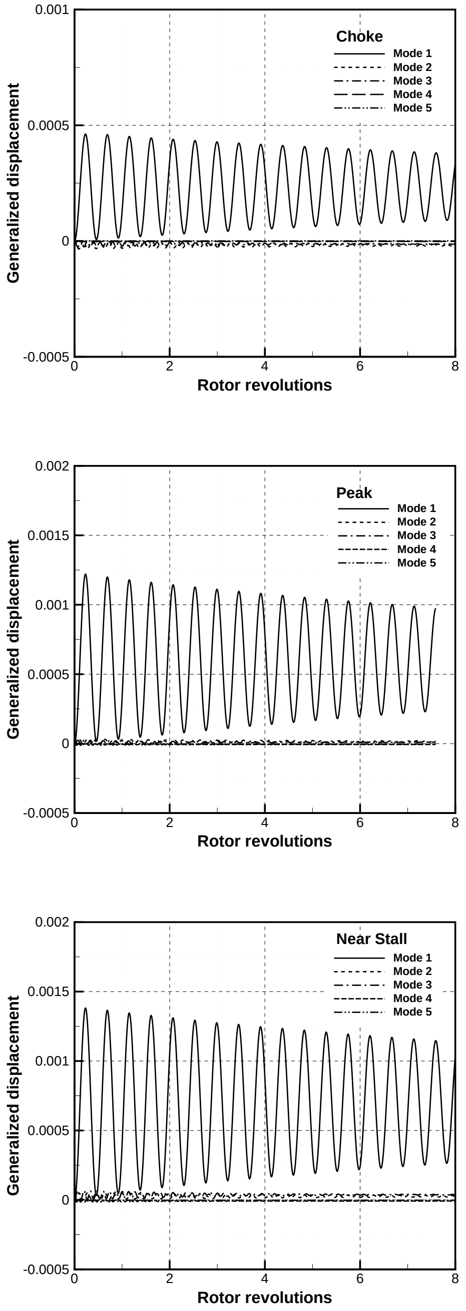

FIGURE 5: The damped responses of blade 2 at choke, peak and near stall

Flutter boundary of the compressor rotor was captured in stall operation. Fig. 8 shows the first 5 modal displacements in the stall flutter. Fig. 9 demonstrates how the rotor blade flutter initiates in higher modes. Occurrence of flutter can be identified with changes in response type from the damped to the divergent, which is captured in higher modes about 2.3 revs. Flutter starts simultaneously for all modes, however the 1st mode has a significantly larger displacement

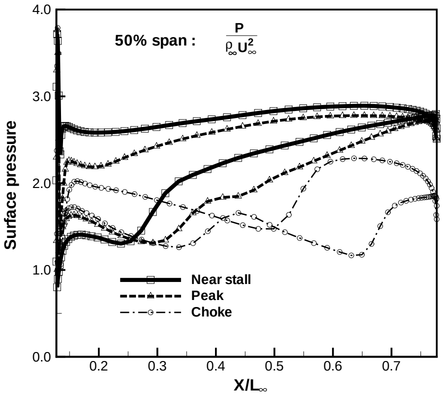

FIGURE 6: Comparison of surface static pressure distributions of NASA Rotor 67

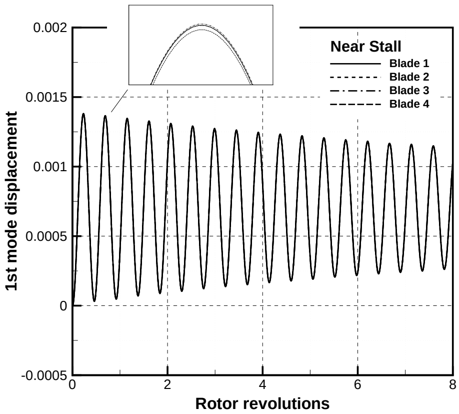

FIGURE 7: Time traces of the 1st mode displacements of NASA Rotor 67 near stall

than the following modes as it develops. Therefore, the effects of higher modes on the stall flutter may not be influential.

After the flutter onset 4 blades experience the transient state with the damped oscillations for about 3 revs. It may be explained by rotating stall inception. In general stall inception develops without flow breakdown for about 2 or 3 rotor revolutions after the onset, and eventually goes into the fully developed rotating stall. The axial symmetry of rotating flow changes to a non-symmetric disturbance at the very beginning of rotating stall. It can lead each blade to vibrate with different amplitudes and phase angles as presented in Fig. 10. After the stall flutter onset, the phase angle increases with diverging oscillations.

Fig. 11 shows the speedline, and flutter boundary is found at point D. Except for the stall operation, the rotor blades die out in terms of time including choke, peak and near stall. When the compressor throttles with the reduction of the mass flow, the pressure ratio of the rotor blades increases from the point A to point C. On the contrary, the ro-

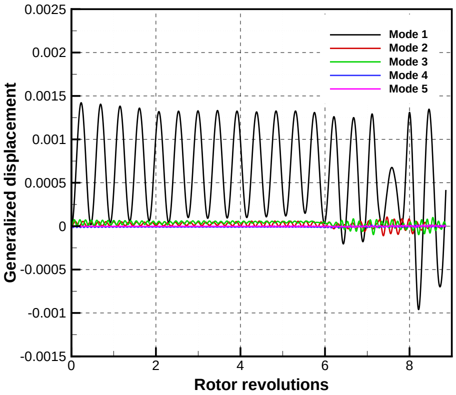

FIGURE 8: Time traces of the generalized displacements of blade 2 in stall flutter

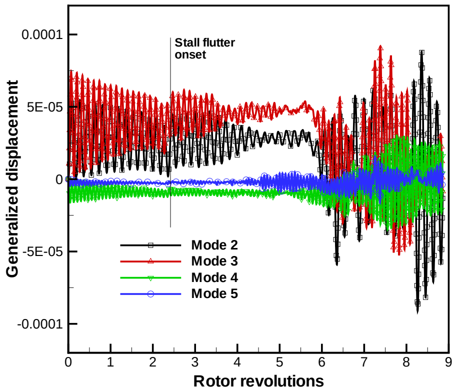

FIGURE 9: Time traces of the 2nd, 3rd, 4th and 5th mode displacements of blade 2 in stall flutter

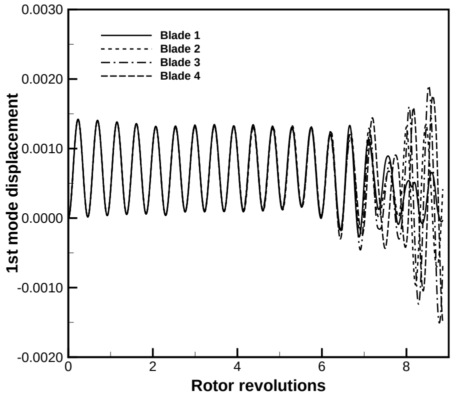

FIGURE 10: Variations of the blade 1st mode displacements in stall flutter

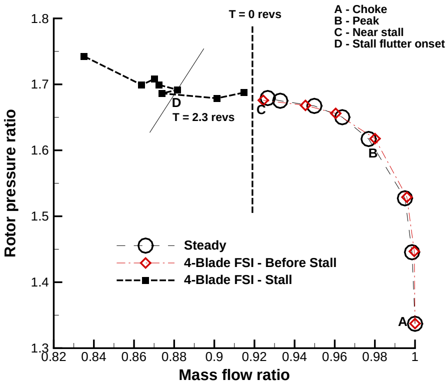

FIGURE 11: The predicted speedline of Rotor 67 by fluid/structure coupled simulation

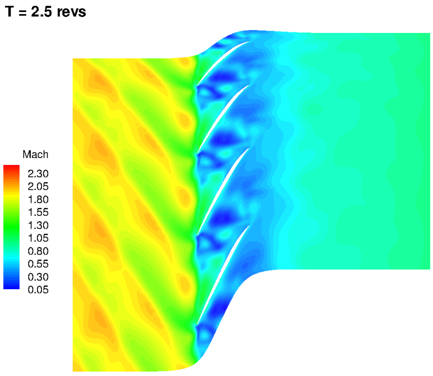

FIGURE 12: Mach number contour of the rotor tip span around flutter onset

tor pressure ratio decreases slightly and then increases from the point D (stall flutter onset). This type of rotating stall can be categorized into the progressive type stall.

Fig. 12 represents Mach number contour of the rotor tip span at 2.5 revs, just after flutter onset. The disturbed flow region due to the flow separation indicates very low Mach number close to zero. The rotor tip passage is usually disturbed partly around the onset of the stall flutter. Rotating stall usually takes place around rotor tip and propagates in the opposite direction of the rotor rotation behind the detached sonic boundary from the rotor blades where the flow is subsonic.

Fig. 13 shows the velocity vector with sonic boundary at the rotor tip span. When the rotor flutter is triggered, the sonic boundary is attached to the rotor leading edge. The flow near the leading edge points out toward the rotor circumferential pitch line with the local flow separation.

Flow instability near the rotor tip may be understood by the fluctuations in the static pressure of the rotor upstream [18, 24, 25] as plotted in Fig. 14. It is obvious that the instability of the upstream flow occurs at 2.3 revs, which corresponds to flutter onset point as captured in Fig. 8, -9.

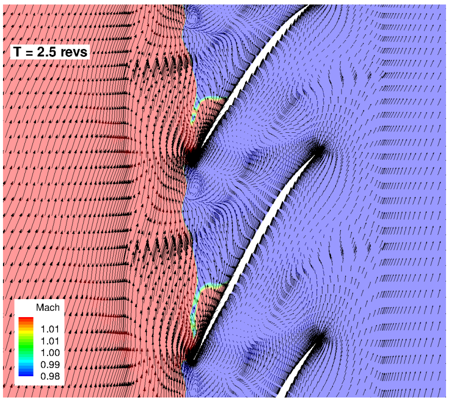

FIGURE 13: Velocity vector of rotor tip section at 2.5 revs with Mach number contour indicating sonic boundary

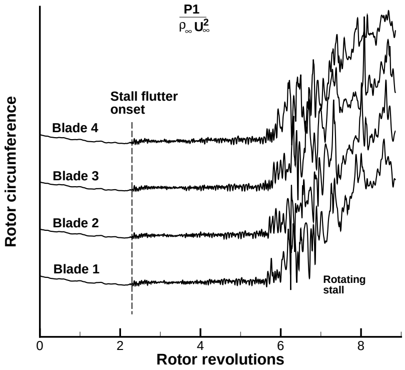

FIGURE 14: Time traces of rotor upstream static pressure at rotor tip span

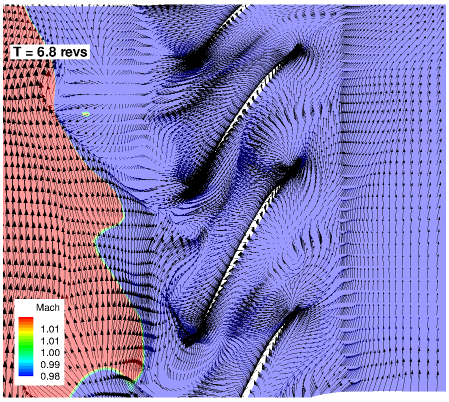

FIGURE 15: Velocity vector of rotor tip section at 6.8 revs with Mach number contour indicating sonic boundary

At 5.7 revs, the fluctuation in the static pressure grows dramatically.

Fig. 15 is velocity vector field at the tip span. As the rotating stall fully develops, the sonic boundary is fully detached from the rotor. The incoming flow toward rotor leading edge is largely disturbed and the rotating instability prop-

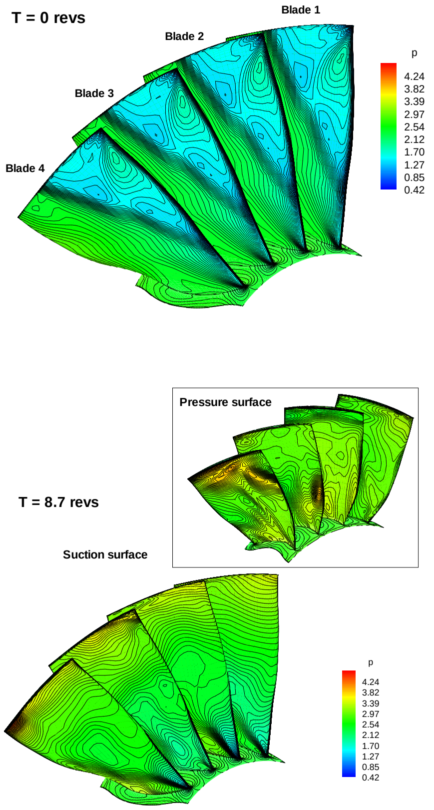

FIGURE 16: Variations in surface static pressure during the stall flutter

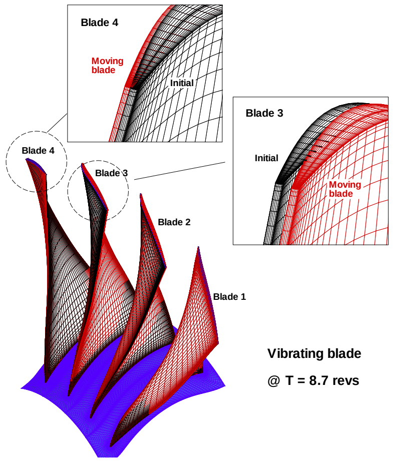

FIGURE 17: Blade vibration at T=8.7 revs

agates toward both upstream of the rotor and the rotor circumferential direction. Needless to day, the highly disordered flows largely contribute to the blade flutter.

Fig. 16 shows static pressure of the suction surface variations during the stall flutter. The strong shocks on the oblique surface at T = 0 revs are distributed in the same manner for all 4 blades, however these disappear at T=8.7 revs. This phenomena can be understood by the detachment of the sonic plane from the blade passages as the stall develops. Static pressure on the pressure/suction surface is nonuniformly distributed for each blade. Hence the blade loading acting on each blade can enforce the blades to flutter in the different phase angles and in the opposite directions.

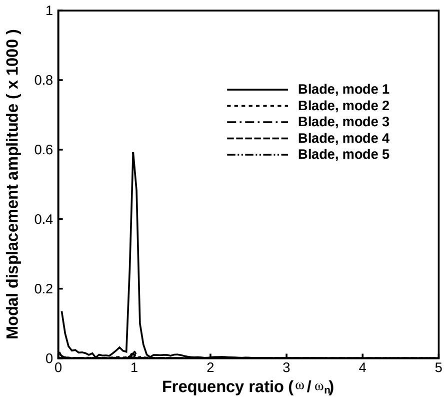

FIGURE 18: Frequency ratio of Rotor 67 stall flutter predicted by FFT

Fig. 17 represents the blade vibration at T=8.7 revs. The blade oscillations are non-periodic and likely non-synchronized since the blade 3 and 4 vibrate in the opposite direction with the different amplitudes.

The frequency of the vibrating blades during the stall flutter was obtained using FFT(fast Fourier transform) analysis. The time traces of modal displacements are used for the FFT input variables. Fig.18 shows frequency ratio ($\frac{\omega}{\omega_n}$) which is defined by the vibration frequency of the blade divided by the blade natural frequency. Resonance occurs at the 1st mode natural frequency of 584.04 Hz. Once the stalled flutter initiated it cannot be stopped in general and gradually diverges. In the current study, the response of the rotor blades amplifies dramatically after a sudden change in the response at about 7 revs as displayed in Fig.8, -9, -10.

7.2 Full Annuls Simulation

Using the full annulus, flutter simulation of NASA Rotor 67 was conducted at peak point in order to prove flutter predictions by using the 4 blade passages with periodic boundary conditions. The full annulus mesh having 22 blade passages was constructed using the same topology and size of the each passage used for the 4 blade FSI simulation as presented in Fig. 3. Total 308 blocks are used for the parallel computations.

Fig. 19 presents the 1st mode displacements of the full annulus NASA Rotor 67. All of 22 blades vibrate showing the damped responses with very similar phase angle and amplitude level.

Fig. 20 shows Mach number contour of the 30% span from the shroud at 5 revs. The λ-shape passage shocks are clearly captured around the leading edge, which is a major feature of the transonic compressor rotor reported by the experiment [15] and other researchers [26, 27]. The flow field

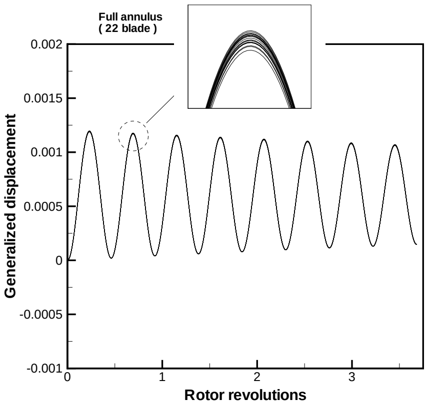

FIGURE 19: The damped responses of full annulus Rotor 67

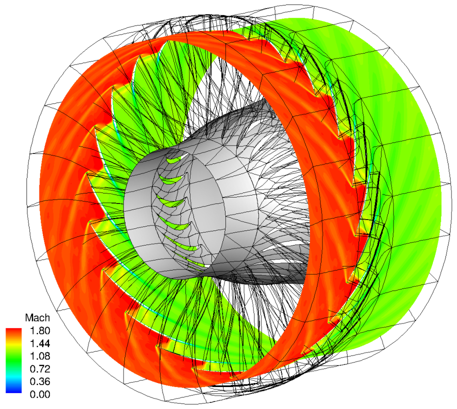

FIGURE 20: Mach number contour of 30% span from the shroud at peak predicted by the full annulus FSI

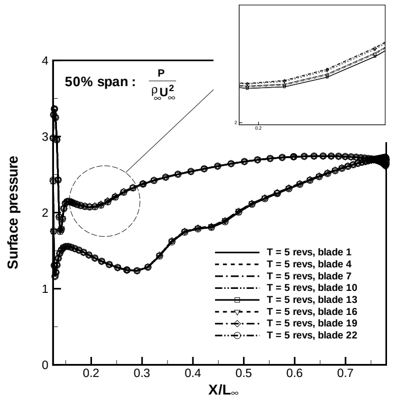

FIGURE 21: Surface pressure distributions of 50% span at peak predicted by the full annulus FSI

of each blade passage predicted by using the fully coupled FSI approach shows very similar pattern along the rotor circumference. The surface pressure distributions at 50% span and the tip span are presented in Fig. 21 and Fig. 22. Obviously 22 blades show identical distributions, and hence each vibrating blade can show periodic behavior.

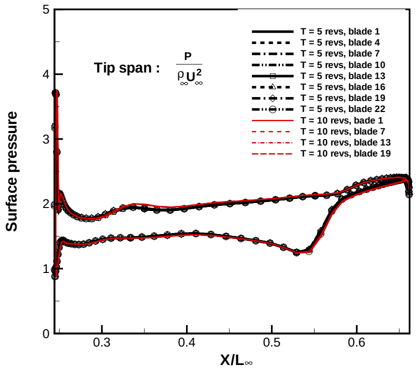

FIGURE 22: Surface pressure distributions of the tip span at peak predicted by the full annulus FSI

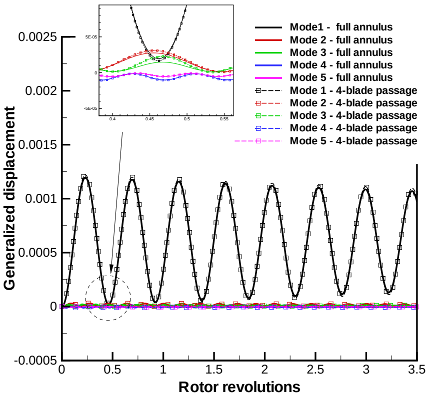

FIGURE 23: Comparison of the modal displacements between the full annulus and the 4-blade passage

Comparison of first two modal displacements for the second blade was illustrated in Fig. 23. The predicted displacements from the full annulus FSI and the 4 blade passage FSI decay in the same manner for the amplitude and phase angle. By taking into account the main objective of the FSI is to find out the flutter boundary at a given or target design condition, the full annulus FSI calculation is not necessary since the 4 blade passage calculation with periodic boundary gives the same results before the stalled flutter.

7.3 Unstalled Flutter in NASA Rotor 67

From the design point of view, it is critical to find flutter boundary using proper parameters. One way to simulate unstalled flutter is to use the parameter, reduced velocity(V^*). The increase of V^* can stand for the increase in freestream dynamic pressure at a certain design point or a given back pressure.

Flutter computations with alternating V^* were performed at near stall condition. Fig. 24 shows 1st mode displacements with $V^* = 0.4357, 0.6357$ and 0.8357. The damped responses are obtained with $V^* = 0.4357$ and 0.6357. However, for $V^* = 0.8357$, the oscillation of the

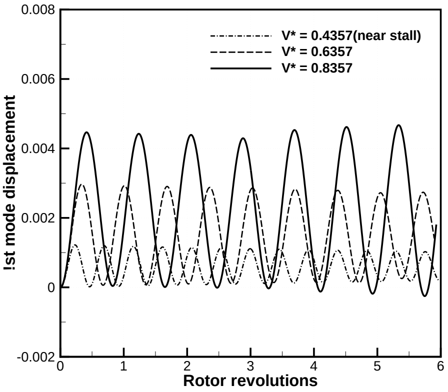

FIGURE 24: Effects of reduced velocity(V^*) on NASA Rotor 67 flutter at near stall

modal displacement diverges with time. It is obvious that flutter boundary locates somewhere between $V^* = 0.6357$ and $V^* = 0.8357$. Unlike the stall flutter where the flow fields largely disturbed due to the massive flow separation, the oscillation of the vibrating blades gradually amplifies like wing flutter.

8 Conclusions

A fully coupled fluid/structure interaction method for axial compressor flutter was developed. An advanced moving mesh technique that can significantly improve the mesh quality over the blade tip was implemented. Using the 4 blade passages of NASA Rotor 67, flutter simulations were conducted from the choke to stall by applying the DES of turbulence with the higher order spatial schemes. Flutter occurs in Rotor 67 as rotating stall develops. Before stall the responses of the rotor blades decay with time, as a consequence no flutter.

The full annulus simulation at peak efficiency condition was performed to verify the multi-passage approach with periodic boundary. It was shown that the multi-passage approach with periodic boundary conditions can be applied to predict flutter boundary of transonic rotor compressors when the flow is unstalled. The frequency analysis indicates that the compressor rotor flutters with the 1st mode resonance in stall operation.

The unstalled flutter of the multi-passage was simulated by increasing the reduced velocity. This approach can faciliate the prediction of the engine flutter under various operating conditions.

Acknowledgement

The grant support from the industrial partners of GUIde Consortium, 09-GUIDE-1010, is acknowledged.

REFERENCES

[1] R. Kamakoti, and W. Shyy, “Fluid.structure interaction for aeroelastic applications,” *Progress in Aerospace Sciences*, vol. 40, pp. 535–558, 2004.

[2] V. Gnesin, and R. Rzadkowski, “A Coupled Fluid-Structure Analysis for 3-D Inviscid Flutter of IV Standard Configuration,” *Journal of Sound and Vibration*, vol. 251, pp. 315–327, 2002.

[3] H. Doi, and J.J. Alonso, “Fluid/Structure Coupled Aeroelastic Computations for Transonic Flows in Turbomachinery.” GT2002-30313,Proceedings of ASME Turbo Expo 2002, 2002.

[4] V. Carstens, R. Kemme, and S. Schmitt, “Coupled Simulation of Flow-srtuctrue Interaction in Turbomachinery,” *Aerospace Science and Technology*, vol. 7, pp. 298–306, June 2003.

[5] A.I. Sayma, M.V. Vahdati, and M. Imregun, “Turbine Forced Response Prediction Using an Integrated Nonlinear Analysis,” *Proceedings of the Institution of Mechanical Engineers, Part K: Journal of Multi-body Dynamics*, vol. 214, pp. 45–60, 2000.

[6] X.Y. Chen, G.-C. Zha, M.-T. Yang, “Numerical Simulation of 3-D Wing Flutter with Fully Coupled Fluid-Structural Interaction,” *Journal of Computers & Fluids*, vol. 36, pp. 856–867, 2007.

[7] P.R. Spalart, W.H. Jou, M. Strelets, and S.R. Allmaras, “Comments on the Feasibility of LES for Wings, and on a Hybrid RANS/LES Approach.” Advances in DNS/LES, 1st AFOSR Int. Conf. on DNS/LES, Greyden Press, Columbus, H., Aug. 4-8, 1997.

[8] H.S. Im, and G.C. Zha, “Delayed Detached Eddy Simulation of a Stalled Flows Over NACA0012 Airfoil Using Higher Order Schemes.” AIAA Paper 2011-1297, Jan. 2011.

[9] G.C. Zha, Y.Q. Shen, and B.Y. Wang, “Calculation of Transonic Flows Using WENO Method with a Low Diffusion E-CUSP Upwind Scheme.” AIAA Paper 2008-0745, 46th AIAA Aerospace Sciences Meeting, Reno, NV, Jan. 2008.

[10] Y.Q. Shen, B.Y. Wang, and G.C. Zha, “Implicit WENO Scheme and High Order Viscous Formulas for Compressible Flows .” AIAA Paper 2007-4431, 2007.

[11] B. Wang, Z. Hu, and G. Zha, “A General Sub-Domain Boundary Mapping Procedure For Structured Grid CFD Parallel Computation,” *AIAA Journal of Aerospace Computing, Information, and Communication*, vol. 5, pp. 425–447, 2008.

[12] P.R. Spalart, and S.R. Allmaras, “A One-equation Turbulence Model for Aerodynamic Flows.” AIAA-92-0439, 1992.

[13] M. Shur, P.R. Spalart, M. Strelets, and A. Travin, “Detached-Eddy Simulation of an Airfoil at High Angle of Attack”, 4th Int. Symp. Eng. Turb. Modelling and Measurements, Corsica.” May 24-26, 1999.

[14] A. Jameson, “Time Dependent Calculations Using Multigrid with Applications to Unsteady Flows Past Airfoils and Wings.” AIAA Paper 91-1596, 1991.

[15] A.J. Strazisar, J.R. Wood, M.D. Hathaway, and

K.L.Suder, “Laser Anemometer Measurements in a Transonic Axial-Flow Fan Rotor.” NASA Technical Paper 2879, November, 1989.

[16] Y. Gong, “A Computational Model for Rotating Stall and Inlet Distortions in Multistage Compressors.” Ph.D. Thesis, Massachusetts Institute of Technology, Feb. 1999.

[17] M. Inoue, M. Kuroumaru, T. Tanino, S. Yoshida, and M. Furukawa, “Comparative Studies on Short and Long Length-Scale Stall Cell Propagating in an Axial Compressor Rotor,” *AMSE J. of Turbomach.*, vol. 123, pp. 24–31, 2001.

[18] D.A. Hoying, C.S. Tan, H.D. Vo, and E.M. Greitzer, “Role of Blade Paggaase Flow Structures in Axial Compressor Rotating Stall Inception,” *AMSE J. of Turbomach.*, vol. 121, pp. 735–742, 1999.

[19] E.C. Yates Jr., “AGARD standard aeroelastic configurations for dynamic response. Candidate configuration I.-wing 445.6 .” NASA-TM-1000492, 1987.

[20] R.V. Goggett, R.V. Rainey, and H.G. Morgan, “An experimental investigsation of Aerodynamic Effects of Airfoil Thickness on Transonic Flutter Characteristics.” NASA TMX-79, 1959.

[21] F. Liu, J. Cai, and Y. Zhu, “Calculation of Wing flutter by a Coupled CFD-CSD method.” AIAA-2000-0907, 2000.

[22] M.A. Bakhle, T.S.R. Reddy, and T.G. Keith Jr., “Time Domain Flutter Analysis of Cascades Using a Full-Potnetial Solver,” *AIAA Journal*, vol. 30, pp. 163–169, 1992.

[23] H. Im, X. Chen, and G. Zha, “Detached Eddy Simulation of Unsteady Stall Flows of a Full Annulus Transonic Rotor.” ASME GT2010-23465, 2010.

[24] I. Day, “Stall Inception in Axial Flow Compressors,” *AMSE J. of Turbomach.*, vol. 115, pp. 1–9, 1993.

[25] T.R. Camp, and I.J. Day, “A Study of Spike and Modal Stall Phenomena in a Low Speed Axial Compressor,” *AMSE J. of Turbomach.*, vol. 120, pp. 393–401, 1998.

[26] I.K. Jennions, and M.G. Turner, “Three-Dimensional Navier-Stokes Computations of transonic Fan Flow Using an Explicit Flow Solver and an Implicit $k-\varepsilon$ Solver,” *AMSE J. of Turbomach.*, vol. 115, pp. 261–272, 1993.

[27] T. Arima, T. Sonda, M. Shirotori, A. Tamura, and K. Kikuchi, “A numerical Investigation of Transonic Axial Compressor Rotor Flow Using a Low-Reynolds-Number k-e Turbulence Model,” *AMSE J. of Turbomach.*, vol. 121, pp. 44–58, 1999.